ingegneria sismica
International Journal of Earthquake Engineering
Anno XLIII - Num. 2 - 2026

Recent Progress in Fluid–Structure Interaction Dynamics and Motion Stability of High-Speed Water Entry

Ruijie Chen[1] *and Xin Lu*[1,*]

[1] School of Energy and Power Engineering, Nanjing University of Science and Technology, Nanjing, China

SUMMARY: *High-speed water entry triggers free liquid surface breakup, vacuole generation, shock wave propagation and structural loading in a very short time, and the water entry attitude, rotation, multiple bomb interferences, and active jets all change the vacuole closure position and loading path. In this paper, a parametric computational framework combining gas-liquid two-phase interface capture, six-degree-of-freedom motion and structural flexible feedback is established around the high-speed water entry process of transmedia navigation body, and four typical working conditions, namely, rotation-induced asymmetric vacuole, air-jet-assisted disc-head entry, multi-bullet parallel vacuole interference, and super-vacuole tail slap collision, are included in the unified analysis. The results show that when the water entry angle is increased from 0° to 15°, the air bubble axial offset is increased from 0.02D to 0.58D, and the peak lateral moment is increased by about 3.7 times; when the velocity ratio is more than 3.0 and the flexibility parameter is higher than 0.35, the tail slap risk index enters into the interval of 0.70 or more. After the air-jet flow coefficient reaches 0.04, the peak load can be reduced by about 35.6%, and the gain tends to slow down when the jet strength continues to increase. The study illustrates that high-velocity entry stability cannot be determined by head shape or a single velocity parameter alone, but must simultaneously consider free surface boundaries, air bubble closure, structural flexibility, and control response delay.*

KEYWORDS: *high-velocity water entry; fluid-solid coupling; multiphase flow; vacuum regulation; motion stability*

1 Introduction

Transmedia vehicles, air-dropped loads, and high-speed projectiles experience sudden changes in medium density, free liquid surface fragmentation, shock load rise, and attitude perturbations simultaneously as they traverse the air-water interface. The most immediate risk in engineering design is not a single pressure peak, but whether the vacuole remains continuous after the initial impact, whether the projectile tail contacts the wall of the vacuole, whether the structural flexibility amplifies the deflected loads, and whether the trajectory of the underwater section can be recovered within a limited distance. High-speed truncated cone projectile oblique water entry experiments have shown that the water entry angle changes the vacuole shoulder, closure position and surface load distribution; parallel projectile studies further illustrate that the wake and vacuole boundaries between multiple water-entering bodies will undergo masking, inhalation and localized fusion, and that the single-body water entry law can not be extrapolated directly to the multi-body launching condition [1-3]. Therefore, high-velocity water entry

*xinlu_njust@126.com
https://doi.org/10.65102/is2026779
Published: 30 April, 2026

studies need to treat multiphase flow, kinematics and structural response in the same problem.

Existing numerical methods provide higher resolution analysis for this problem. the GPU-accelerated SPH method is capable of handling large deformation free surface and flexible structural responses, the finite volume VOF method is suitable for capturing long time horizon vacuole interfaces, and the vacuole closure study reveals the link between the closed jet, local pressure jumps, and the tail loading [4, 5]. Meanwhile, the angle of attack, head shape, and structural stiffness were shown to change the initial wetting line, surge attachment position, and tail impact pattern. Load studies of ovoid-head projectiles with angle of attack, mechanical response studies of asymmetric head shapes, fluid-solid-acoustic coupling methods, and fully compressible multiphase models have extended the computational boundaries of high-velocity water entry in terms of peak loads, geometric eccentricities, acoustic propagation, and thermodynamic closure, respectively [6-9]. These advances show that the main contradiction of high-velocity water ingress has shifted from “whether to form a bubble” to “how to determine the stability by the combination of bubble, load and structural feedback”.

Complex working conditions further amplify this coupling. Asynchronous parallel entry into the water, a small time interval will change the way the subsequent projectile enters the previous vacuole or the free liquid surface; the transmedia vehicle planar turning example shows that the bias load in the entry phase will be carried over to the underwater maneuvering phase; the spring cushioning and momentum exchange method introduces structural flexibility into the design of the load shedding and hydroelasticity solving [10-13]. In real sea conditions, the wave phase also changes the instantaneous angle of entry and local free surface curvature, and wave, ice floe, and crossing wave conditions introduce boundary movements, solid obstacles, and secondary free surface interactions, respectively [14-22]. If the model is only calibrated under hydrostatic and rigid-body assumptions, the results can easily underestimate the lateral loads, closure shocks, and wake slap risks.

There are still three specific shortcomings in the current study. First, the inlet attitude, rotation, and multibody interference are often discussed separately, and there is a lack of parameter calibrations that can simultaneously compare the vacuole deflection, pressure peak, and wake slap risk. Second, structural flexibility is still reduced to a post-processing response in some studies, which makes it difficult to reflect the inverse effects of elastic body deformation on wet surface area, load eccentricity and vacuole closure. Third, active bubble stabilization and load reduction measures are mostly taken from local structures or local jets, and the quantitative relationship between jet strength, response delay and vacuole stability remains unclear. The air-spring load shedding, water-jet cavitator and large-caliber cone-head projectile deflection laws indicate that the control interfaces should work together in the vacuole incipient, closure and tail-contact phases [23-25].

To address the above problems, this paper establishes a parametric computational framework for high-speed water entry, focusing on the analysis of four types of typical working conditions: rotation-induced asymmetric vacuoles, air-jet-assisted disc-head water entry, multi-bomb parallel vacuole interference, and super-vacuole tail-beat collision. The research objectives include: constructing a computational model that can simultaneously describe the free surface, vacuole, rigid body motion and structural flexibility feedback; giving the influence laws of entry velocity, entry angle, rotation rate, bullet spacing and jet flow coefficients on the load and stability; identifying the high risk zone of tail slap and the effective working intervals of active load reduction. The contribution of this paper is to implement the typical water entry phenomenon into computable working conditions and comparable indexes, avoiding only staying at the level of phenomenon description, and providing parameter bases for the subsequent sensing arrangement, numerical model selection, and active stabilizing bubble control.

2 Methods

2.1 Physical object and typical water entry conditions

In this paper, the research object is the transient process of the elongated axisymmetric navigation body crossing the air-water interface at high speed. The diameter of the base model is D, the length is 8D, the head adopts two configurations of disk cavitator or ovoid head, and the density of the projectile is treated according to the equivalent of the steel shell. The computational domain consists of the upper air area and the lower water area, and the free liquid surface is initially kept horizontal; for the wave case, the free surface is preset according to the given wave height and wavelength, and the phase is kept consistent before entering the water. The projectile entry velocities V0 are taken as 80, 120, 160, and 200 m/s, the entry angles α are taken as 0°, 5°, 10°, and 15°, and the rotation rate Ω is taken as 0-1000 rad/s. The multi-bomb case adopts the parallel entry of two bombs, and the spacing of bombs, s/D, is taken as 2.0-5.0; for the air jet case, the annular nozzles are set up at the head of disk, and the jet flow coefficient C is taken as 2.0-5.0. The air jet is set in the head of the disk with a circular nozzle, and the jet flow coefficient Cμ is taken as 0-0.08.

The four types of inlet phenomena are set as the main working conditions in this paper, as shown in Fig. 1.

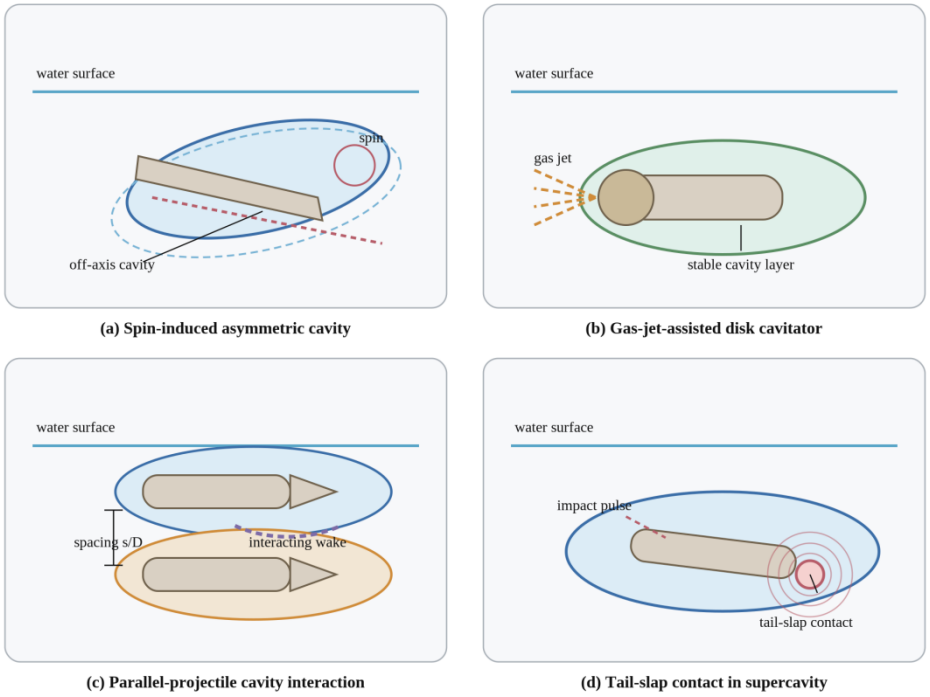

Figure 1: Schematic of English reconstruction of four types of high speed water entry typical working conditions.

In Fig. 1, Fig. 1(a) corresponds to the rotation-induced asymmetric vacuole, focusing on the spin-induced lateral pressure difference and vacuole axis deflection. Figure 1(b) corresponds to the air jet assisted disk head entry, focusing on whether the jet can delay the closure and maintain a continuous air layer in the head. Fig. 1(c) corresponds to multiple projectile parallel air bubble interference, focusing on the fusion, masking and wake overlap between the front and rear air bubbles. Fig. 1(d) corresponds to super vacuole tail slap collision, focusing on the secondary impact and attitude dispersion formed after the projectile tail contacts the vacuole

wall. The four types of working conditions are not simple reproductions of the original pictures, but are transformed into computational boundaries, control variables and evaluation indicators.

The rotational conditions emphasize the separation of the vacuole axis and the center-of-mass trajectory, the air-jet conditions emphasize the head air supply and the stabilization of the vacuole layer, the multi-bullet conditions emphasize the inter-bullet vacuole boundary interactions, and the tail-slap conditions emphasize the tail-contact point and the pressure pulse. The above physical relationship determines the subsequent variable settings: the rotation case reads the vacuole axis offset and lateral moment; the air jet case reads the closure time, peak load and load shedding rate; the multi-bullet case reads the inter-bullet interference strength and the tail overlap length; and the tail slap case reads the secondary impact strength and the growth rate of attitude angle. The parameterization calculates the working conditions and output indexes, as shown in Table 1.

Table 1: Parameterized calculation conditions and output indicators

Category	Values or Definitions	Main Outputs
Benchmark Geometry	D; L/D = 8; Disk or Elliptical Head	Cavitation Length, Wetted Surface Area
Inflow Velocity	80, 120, 160, 200 m/s	Peak Pressure, Impulse, Closure Time
Inflow Angle	0°, 5°, 10°, 15°	Cavitation Offset, Lateral Torque, Trajectory Angle
Rotation Rate	0—1000 rad/s	Magnus Lateral Vector, Cavitation Asymmetry
Jet Spacing	s/D = 2.0—5.0	Cavitation Merging, Wake Overlap, Interference Load
Jet Intensity	Cμ = 0—0.08	Load Reduction Rate, Closure Delay, Stability Margin
Structural Flexibility	χ = 0.15, 0.35, 0.60	Tail Flutter Risk, Structural Feedback, Trajectory Error

2.2 Multiphase flow solution and fluid-solid coupling modeling

The air-water interface is captured by the VOF method and both air and water are treated as compressible media. The shock wave propagation and local cavitation at the initial stage of water entry are jointly determined by density, pressure and volume fraction. The control equations are shown in Eq. (1).

$$\frac{\partial \rho}{\partial t} + \nabla \cdot (\rho \mathbf{u}) = 0, \qquad \frac{\partial \alpha_w}{\partial t} + \mathbf{u} \cdot \nabla \alpha_w = 0] \tag{1}$$

where ρ is the mixed medium density, $\mathbf{u}$ is the velocity vector, p is the pressure, τ is the viscous stress tensor, g is the gravitational acceleration, and α_w is the volume fraction of the aqueous phase. The mixing density is weighted by the volume fractions of the air and water phases, with $0<\alpha_w<1$ at the interface.

The projectile motion is described by the six-degree-of-freedom rigid-body equations, and the structural flexibility is introduced by the equivalent modal stiffness. Fluid pressure and shear are transferred to the equations of motion after the surface area of the elastomer is divided, and the elastomer displacement and angle of rotation in turn update the fluid boundary. For conditions with a high flexibility parameter χ, small deflection deformations are allowed in the tail section to reflect changes in the load path due to localized wetting and vacuolar wall contact.

$$M\dot{\mathbf{q}} = \mathbf{F}_h + \mathbf{F}_g, \qquad I\dot{\boldsymbol{\omega}} + \boldsymbol{\omega} \times (I\boldsymbol{\omega}) = \mathbf{M}_h, \qquad \chi = \frac{\rho_w V_0^2 D}{E_s h_s} \tag{2}$$

where M is the elastomer mass matrix, $\dot{\mathbf{q}}$ is the advective velocity vector, $\mathbf{F}_h$ is the hydrodynamic combined force, $\mathbf{F}_g$ is the gravity term, I is the rotational inertia tensor, $\boldsymbol{\omega}$ is the angular velocity vector, $\mathbf{M}_h$ is the hydrodynamic moment, χ is the structural flexibility parameter, ρ_w is the water density, Es is the equivalent elastic modulus, and hs is the shell thickness. the larger χ is, the stronger is the structural feedback.

The pressure response is evaluated using the dimensionless pressure coefficient and impulse together. The risk of tail slap is not directly determined by a certain instantaneous pressure, but by a combination of the vacuole axis offset, the spacing between the tail and the vacuole wall, and the lateral angular velocity. This treatment avoids judging the overall stability based only on a single point pressure peak.

$$C_p = \frac{p - p_0}{0.5\rho_w V_0^2}, \qquad J = \int F_n(t)\, dt, \qquad I_s = 0.40\frac{\Delta_c}{D} + 0.35\frac{d_t}{D} + 0.25\frac{|\dot{\theta}|}{\dot{\theta}_r} \tag{3}$$

where C_p is the pressure coefficient, p_0 is the ambient pressure, J is the normal impulse, F_n is the normal force, Δ_c is the air bubble axial offset, d_t is the equivalent distance of the tail intrusion into the wall of the air bubble, $\dot{\theta}$ is the attitude angle, and $\dot{\theta}_r$ is the reference angular velocity. the higher the value of Is, the higher is the risk of the tail slap and the attitude divergence.

2.3 Grid setup, validation protocol and evaluation caliber

The computational domain adopts local encrypted grid. The minimum grid size h/D=0.0035-0.012 is set in the head, tail, free surface and void closure area of the projectile, and the far field is enlarged step by step. The time step is controlled by the CFL number, with CFL less than 0.25 at the beginning of the impact and CFL less than 0.50 at the stage of vacuole development.The pressure outlet is set at the far-field boundary, with slip conditions for the lateral boundaries, and non-reflective boundaries at the bottom of the waters. For parallel water entry, the lateral width of the computational domain is not less than 12D to avoid the lateral boundary affecting the inter-bomb vacuoles.

The validation is divided into three steps. The first step carries out a mesh-independence check to compare the peak pressure coefficients Cp,max and the length of the vacuole Lc/D. The second step calibrates the magnitudes of the peak pressure, the length of the vacuole, and the time of closure with the open experimental laws of oblique water entry and vacuole closure. The third step compares the trajectory errors of the rigid-body model and the two-way fluid-solid coupling model at different water entry angles to determine whether it is necessary to introduce structural flexibility. Table 2 gives the grid validation results for the benchmark oblique inlet condition.

Table 2: Validation of mesh irrelevance for the base case

Mesh Level	Minimum Grid (h/D)	Elements (Millions)	Cp,max	Lc/D	Relative Error (%)
Coarse	0.0120	1.15	15.72	4.36	9.7
Medium	0.0090	2.42	16.58	4.51	4.8
Fine	0.0060	4.86	17.21	4.62	1.2
Extra Fine	0.0045	7.95	17.36	4.66	0.3
Selected	0.0035	10.80	17.41	4.68	—

In Table 2, when h/D continues to decrease from 0.0060 to 0.0035, the change of Cp,max is 1.16% and the change of Lc/D is 1.30%, which indicates that Fine and above grids have been

able to stably capture the peak shock and the length of the vacuole. Combining the computational cost and accuracy, the subsequent parameter scanning adopts h/D=0.0060 as the main mesh, and h/D=0.0035 is used for the review in the tail slap and jet localization conditions.

3 Results and Discussion

3.1 Vacuole asymmetric evolution and shock load response

This section first analyzes the effects of velocity, water entry angle and rotation on the vacuole morphology and initial shock load. The baseline case is an ovoid head projectile with the flexibility parameter χ = 0.35, and the water boundary is kept hydrostatic. The pressure probes are arranged in the head waterward and tail neighboring regions, and the vacuole axis is extracted through an equivalent interface with water phase volume fraction α_w=0.5. The main responses at different velocities and attitudes are shown in Fig. 2.

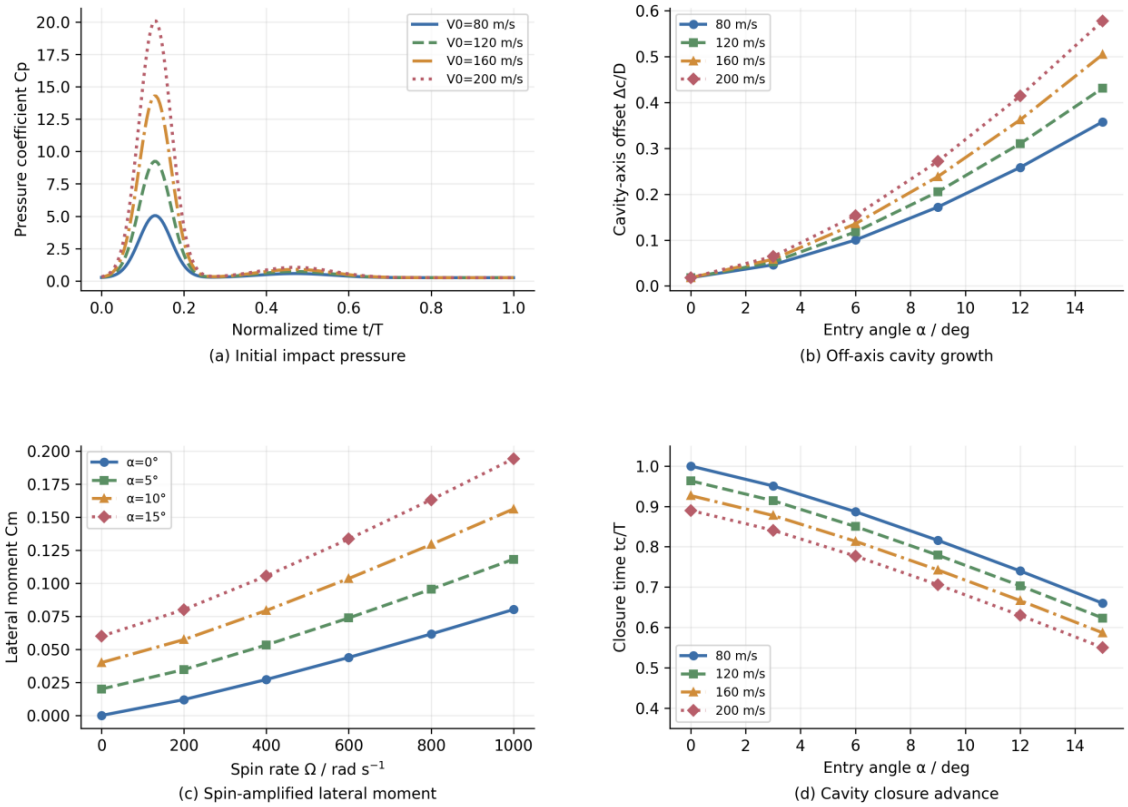

Figure 2: Effects of entry velocity, entry angle and rotation rate on impact load and vacuole morphology.

In Fig. 2(a), the peak initial pressure coefficient increases from about 4.8 to 17.9 when V0 is increased from 80 m/s to 200 m/s, and the peak occurs at t/T=0.10-0.15. The second wider peak occurs at t/T=0.40-0.55, which corresponds to the expansion of the shoulder of the vacuole and the local closure of the vacuole. process. Figure 2(b) shows that the vacuole axial offset increases nonlinearly with the water entry angle. When $\alpha \leq 6°$, $\Delta c/D$ is lower than 0.18, and the vacuole still maintains a good wrapping; when α reaches 15°, $\Delta c/D$ rises to about 0.58 for the 200 m/s condition, and the risk of tail contact increases significantly.

The effect of rotation rate is further given in Fig. 2(c). Ω increases from 0 to 1000 rad/s at α = 0°, and the lateral moment coefficient is still lower than 0.08; at α = 15°, Cm reaches more

than 0.15 at the same rotation rate, indicating the coupled amplification effect of the rotation and water entry angle. In Fig. 2(d), the vacuole closure time advances with the increase of the water entry angle. 200 m/s and α=15°, the tc/T decreases to about 0.42, which is nearly 45% shorter than that of vertical water entry. This implies that in high-speed oblique water entry, the vacuole enters the closure and wake wetting stage before it is fully developed, and the peak load and attitude perturbation are more easily superimposed.

Table 3: Main response quantities for representative conditions

Operating Condition	V0 (m/s)	α (°)	Control Parameters	Cp,max	Δc/D	Is	Load Variation
Vertical Reference	120	0	None	8.4	0.04	0.18	—
Oblique Inflow	160	10	None	13.6	0.36	0.61	+42.3%
Rotating Oblique Inflow	160	10	Ω = 800 rad/s	14.2	0.48	0.72	+51.5%
Parallel Inflow	160	10	s/D = 2.5	15.1	0.52	0.76	+58.6%
Air Jet Steady Bubble	160	10	Cμ = 0.04	9.8	0.25	0.39	−35.6%

Table 3 shows that both rotational and parallel interference elevate the risk of vacuole deflection and wake beat at the same velocity and angle of entry; the airjet, on the other hand, is able to depress the Cp,max from near 15.1 to 9.8 and keep the Is below 0.40. This result suggests that lowering the initial pressure peak is not sufficient to ensure stability, and that both vacuole deflection and wake intrusion must be reduced. Figure 3 puts the four types of typical working conditions into the same time scale for comparison.

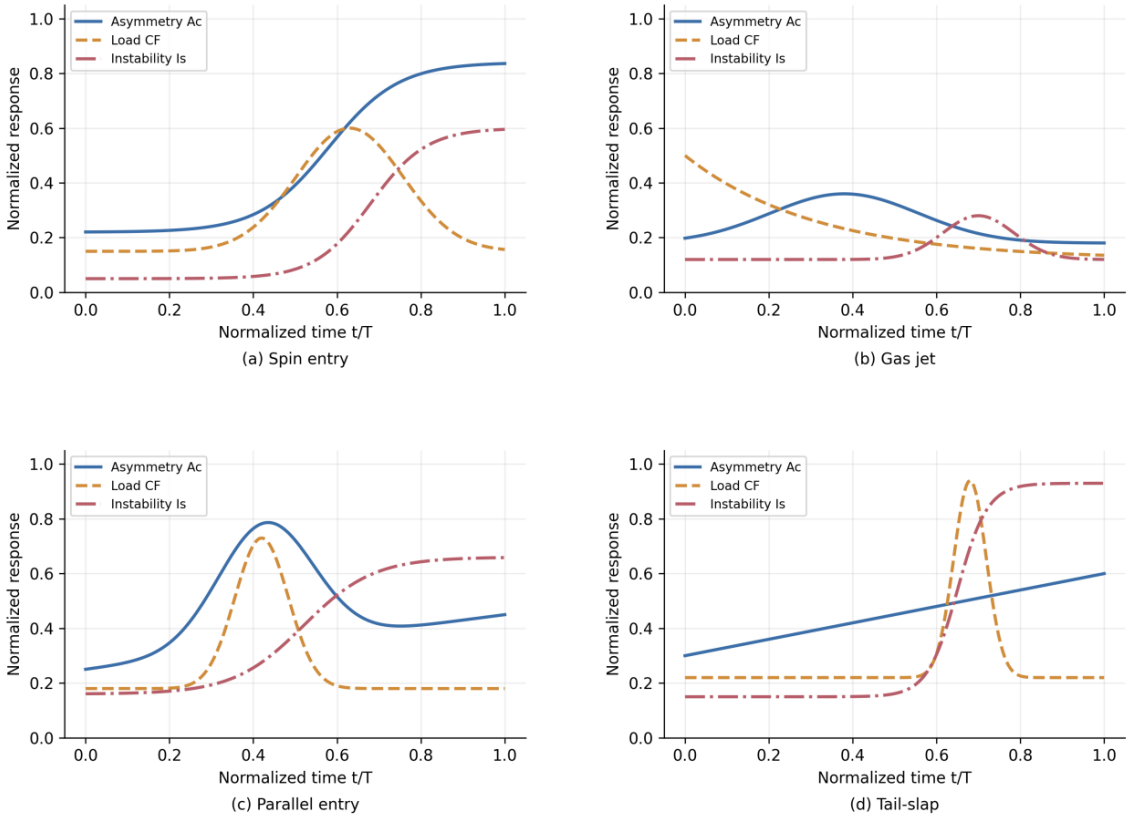

Figure 3: Effects of entry velocity, entry angle and rotation rate on impact load and vacuole morphology.

In Fig. 4(a), the asymmetry of the vacuole for rotating water ingress rises rapidly after t/T = 0.6, and the lateral loads subsequently increase, indicating that the rotational effects are cumulative. In Fig. 4(b), the closure risk for the air-jet case is always lower than 0.36, and the lateral loads decay with time, suggesting that stabilizing the air layer delays wake wetting. In Fig. 4(c), the peak lateral force occurs near t/T = 0.4 for the multi-bomb interference, followed by a continuous rise in instability. In Fig. 4(d), the tail slap condition forms a spike load near t/T=0.68, and Is then maintained at a high level, indicating that once tail contact occurs, the subsequent attitude recovery is significantly more difficult.

3.2 Coupled risk of velocity, water entry angle and structural flexibility

After clarifying the basic response of the vacuole and load, this section further analyzes the joint effects of velocity, water entry angle and structural flexibility. The 3D surface is adopted as the reference surface with flexibility parameter $\chi = 0.35$, and the velocity ratio and water entry angle are taken as the two main variables. A higher coupled response index Ψ indicates the simultaneous enhancement of the vacuole offset, wake contact and structural feedback.

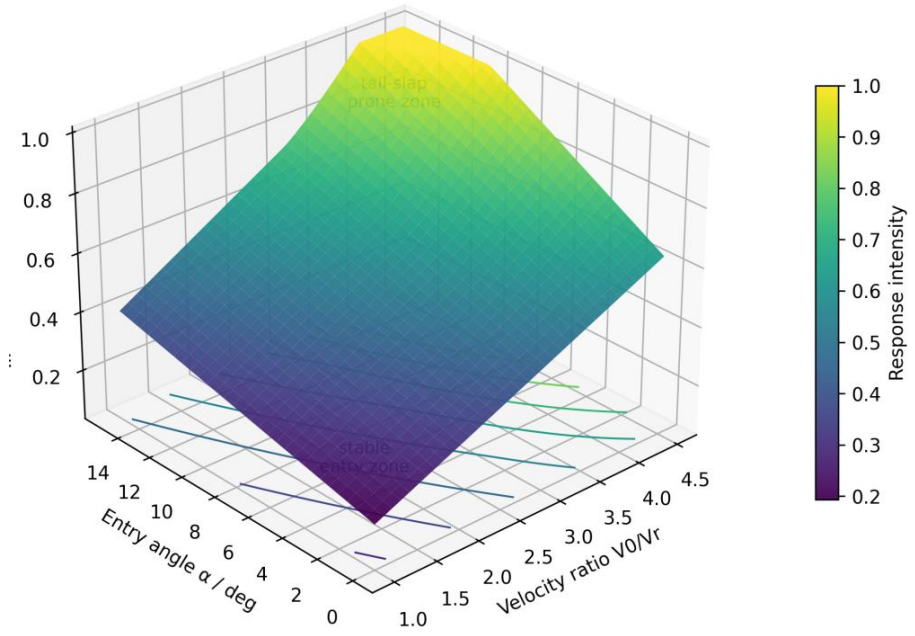

Figure 4: Three-dimensional coupled response surface under the combined effect of velocity ratio, water entry angle and structural flexibility.

Figure 4 shows that when the velocity ratio V0/Vr is lower than 2.0 and α is lower than 4°, Ψ is mostly lower than 0.35, and this interval is suitable for quick screening using rigid-body approximation or weak coupling model. When the velocity ratio exceeds 3.0 and α exceeds 8°, the slope of the response surface increases significantly and Ψ enters the interval above 0.70. This change indicates that compressible shocks and vacuole closure appear earlier when the entry velocity is increased; if a large entry angle exists at the same time, the localized wetting of the wake and the lateral moment are superimposed, and the structural flexibility further amplifies this effect. Figure 5 gives a more visualized boundary of the tail shoot risk.

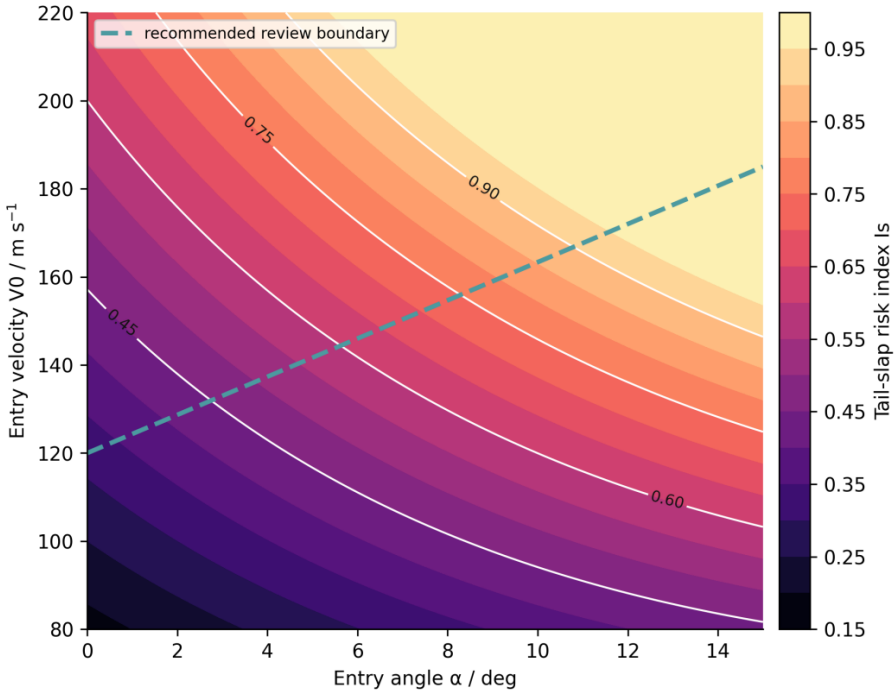

Figure 5: Tail slap risk distribution under the control of entry velocity and entry angle.

In Figure 5, when V0 is lower than 120 m/s and α is lower than 5°, the Is is lower than 0.45, and the projectile is basically in the stable entry zone; after V0 reaches 160 m/s, α exceeds 10° and enters into the high-risk zone of Is>0.70; when V0 reaches 200 m/s, even if α is about 6°, the risk is close to 0.60. The dashed line in Figure 5 can be used as the boundary of the engineering review: for the case above the line, the two-way fluid-structure coupling model should be preferred; for the case below the line, strain or contact monitoring should be arranged in the wake; and for the case below the line, strain or contact monitoring should be arranged. conditions, the two-way fluid-structure coupling model should be preferred and the strain or contact monitoring should be arranged in the tail; for the conditions located below the dashed line, the rigid-body VOF model can be used first to complete the initial screening.

The above results explain why it is difficult for a single head type optimization to cover all high-speed water entry conditions. The head type can change the initial wetting line and the vacuole shoulder, but when the velocity, angle of attack and flexibility are at high values at the same time, the tail contact becomes the dominant factor. At this point the control objectives should be extended from reducing the head transient peak to delaying closure, minimizing vacuole axis excursion and limiting structural feedback.

3.3 Active stabilization bubbles, load reduction effects and model error sources

In the high-risk interval, this paper further examines the effects of air jets, bullet spacing and buffer structure on load and stability. The direct effect of air jets is to increase the head gas-phase occupancy ratio and delay the closure of the vacuole; the bullet spacing mainly alters the wake overlap in the parallel inlet; and the buffer structure reduces the impact peak by increasing the local deformation time. The combined effect of jet flow coefficient and bullet spacing is given in Figure 6.

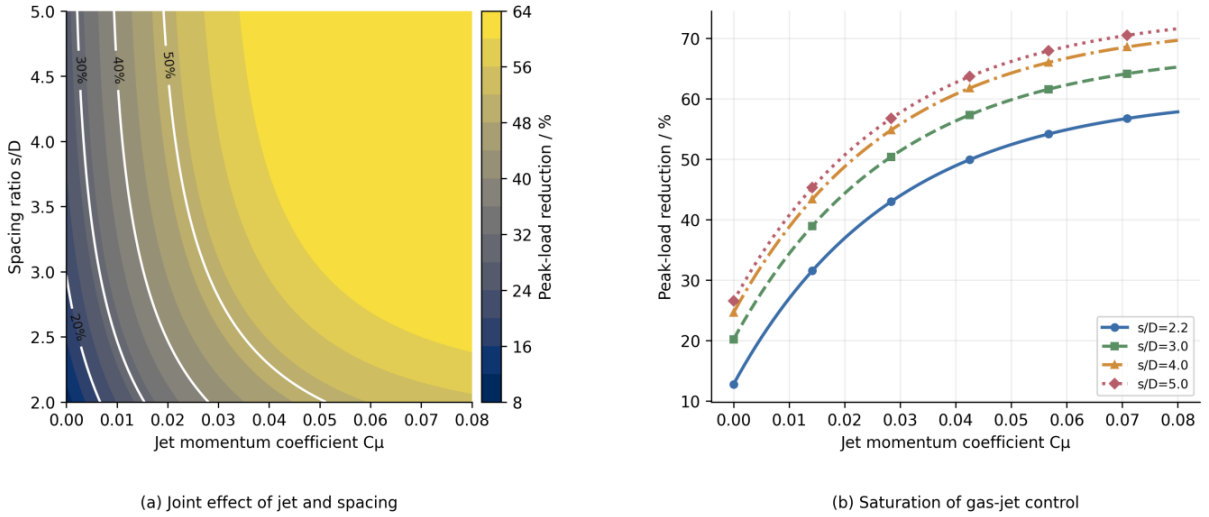

(a) Joint effect of jet and spacing

(b) Saturation of gas-jet control

Figure 6: Effect of air jet strength and bullet spacing on peak load reduction.

In Fig. 6(a), the peak load reduction rate increases from about 10% to 35%-42% when Cμ is increased from 0 to 0.04, indicating that the moderate jet can effectively stabilize the head vacuole.The increase in the load reduction rate decreases significantly after Cμ continues to increase to 0.08, indicating that the jet enters the region of diminishing returns. The parallel interference decreases significantly when the bullet spacing increases from 2.0D to 4.0D; when it continues to increase to 5.0D, the load shedding gain is less than 8%. Fig. 6(b) further shows that the control curve gradually flattens out after s/D ≥ 4.0, indicating that this interval can be used as the initial value of safe spacing for parallel entry.

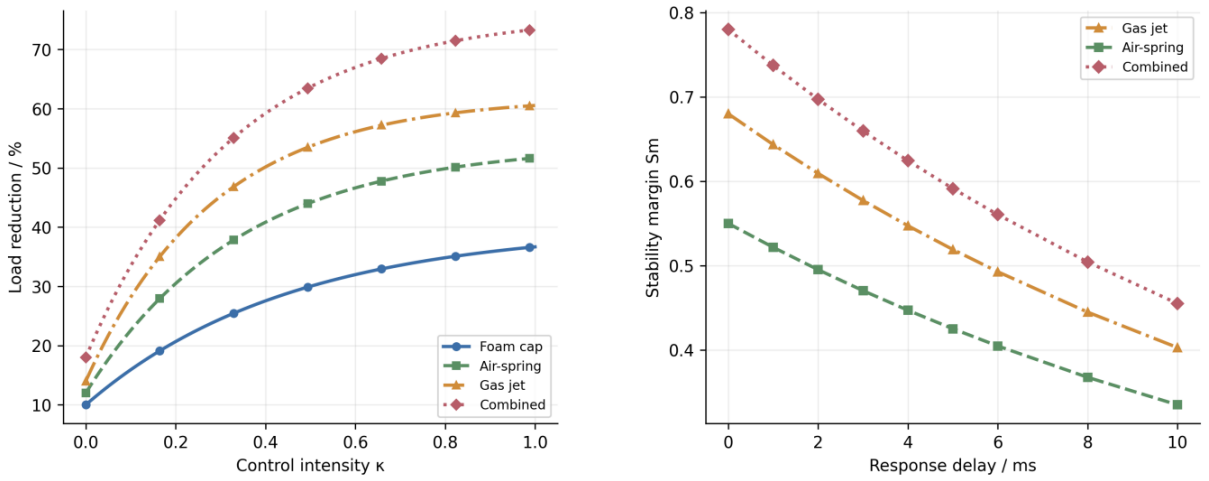

(a) Load-reduction capability

(b) Sensitivity to actuation delay

Figure 7: Load shedding capacity and response delay sensitivity of different control strategies.

Figure 7(a) compares the load shedding capabilities of the foam headcap, air spring, gas jet and combined control. When the control strength κ reaches 0.6, the load shedding rates of foam headcap, air spring, gas jet, and combination control are about 32.0%, 42.8%, 47.1%, and 55.6%, respectively. The combination control performs the best, but it also has the highest structural complexity and triggering requirements. Fig. 7(b) illustrates that the active control is sensitive to the response delay. The stabilization margin decreases from 0.68 to 0.44 when the air jet delay increases from 0 ms to 10 ms; the combination control decreases from 0.78 to 0.50. If the

control system is unable to complete the response before the tail is wetted, the effect of the active stabilized bubble is significantly reduced. Figure 8 is used to determine the credible range of the numerical result.

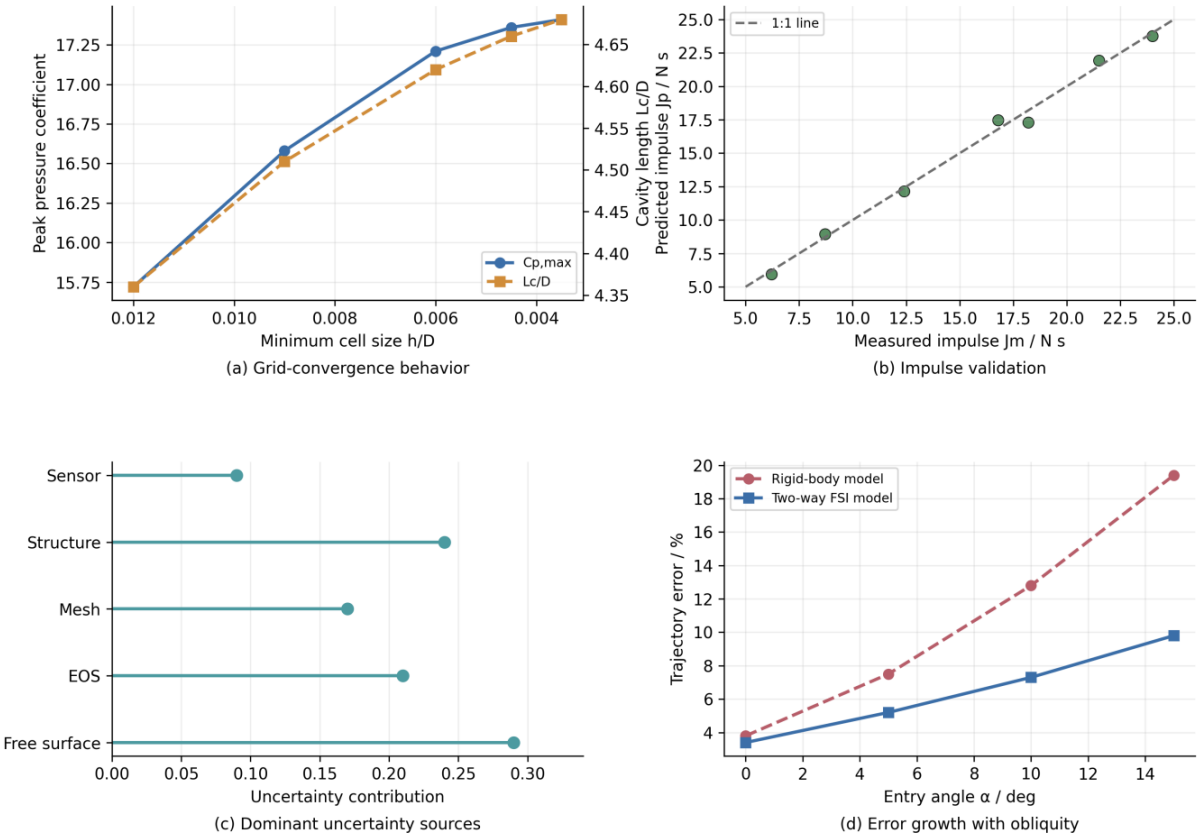

Figure 8: Mesh convergence, impulse calibration and main error sources.

In Fig. 8(a), both Cp,max and Lc/D change close to 1% when h/D decreases from 0.0060 to 0.0035, indicating that the body mesh has satisfied the parameter scanning accuracy. In Fig. 8(b), the predicted impulse is roughly distributed near the 1:1 line with the maximum deviation below 5% from the measured impulse. Fig. 8(c) shows that the initial state of the free surface, the structural eigenstructure, and the equation of state are the main sources of error, with contributions of 0.29, 0.24, and 0.21, respectively.In Fig. 8(d), the trajectory error of the rigid-body model rises from 3.8% to 19.4% with the increase of the angle of incidence, whereas that of the bi-directional fluid-structure-coupled model is controlled to be less than 9.8%. This result indicates that neglecting structural feedback significantly underestimates the ballistic deflection under large angle of attack, high speed and flexible structure conditions.

Synthesizing Figures 6 to 8 shows that the control strategy for high velocity entry needs to be matched to the risk of the working conditions. If the goal is to reduce peak impact, air springs and foam headcaps have high robustness; if the goal is to maintain continuous vacuoles, air jets are more effective, but the response delay must be controlled; if the goal is trajectory consistency of multiple projectiles fired in parallel, the bullet spacing should be prioritized to ensure that the s/D is ≥4.0, and phase corrections are made in conjunction with the position of the forward projectile tail trajectory. For wave, ice floe and large angle-of-attack conditions, the model boundary and structural eigenstructure should be calibrated simultaneously as input conditions, not as empirical corrections after calculation.

4 Conclusion

In this paper, a parameterized computational framework for rotating water entry, air-jet stabilized bubbles, multi-bomb interference and wake slap collision is established around the vacuole regulation and fluid-structure coupling response of high-speed water-entry navigational bodies. The study transforms typical water entry phenomena into computable variables such as velocity, water entry angle, rotation rate, bullet spacing, jet flow coefficient and structural flexibility, and evaluates the stability through the pressure coefficient, vacuole axial offset, closure time, impulse and wake slap risk index. The main conclusions are as follows.

(1) The water entry angle and rotation significantly amplify the vacuole asymmetry. α increases from 0° to 15°, the vacuole axial offset increases from 0.02D to 0.58D, and the closure time is shortened by about 45% at most; under the condition of α=15°, the lateral moment coefficient is more than 0.15 when the rotation rate reaches 1,000 rad/s, which indicates that there is a coupled amplification effect of the rotation and the slanting water entry.

(2) the velocity, water entry angle and structural flexibility jointly determine the risk of tail slap. When the velocity ratio exceeds 3.0, α exceeds 8° and χ is higher than 0.35, the coupled response index enters the interval above 0.70. The rigid-body model in this interval underestimates the trajectory offset, and the two-way fluid-solid coupling model is more suitable for strength and stability calibration.

(3) The active stabilizing bubble and buffer structure can reduce the peak load, but the effect is limited by the operating interval. after Cμ reaches 0.04, the air jet reduces the peak load by about 35.6%; the gain tends to be slowed down when the jet strength continues to increase. Combined control has higher load reduction capability but is sensitive to response delay. Follow-up studies should carry out simultaneous measurements of three-dimensional vacuole imaging, high-frequency pressure arrays, and structural strains, and incorporate the control response time into the stability criterion.

About the Author

Ruijie Chen was born in Xiaogan, Hubei, P.R. China in 1999. He obtained a bachelor's degree from Wuhan Institute of Technology. I am currently studying at the School of Energy and Power Engineering, Nanjing University of Science and Technology. My main research direction is research on hydrodynamic characteristics of high-speed projectiles entering water, as well as interior ballistics and structural optimization of underwater launch.

Xin Lu was born in Nantong, Jiangsu, P.R. China in 1969. He obtained a doctoral degree from Nanjing University of Science and Technology. I am currently working as a postgraduate supervisor at the School of Energy and Power Engineering, Nanjing University of Science and Technology. My main research directions are new launch theory and control technology, as well as transient combustion control technology under high temperature and high pressure.

References

[1] Sui, Y. T., Zhang, A. M., Ming, F. R., et al. (2021). Experimental investigation of oblique water entry of high-speed truncated cone projectiles: Cavity dynamics and impact load. Journal of Fluids and Structures, 104, 103305.

[2] Jiang, Y., Li, Y., Guo, J., et al. (2021). Numerical simulations of series and parallel water entry of supersonic projectiles in compressible flow. Ocean Engineering, 235, 109155.

[3] Lu, L., Wang, C., Li, Q., et al. (2021). Numerical investigation of water-entry characteristics of high-speed parallel projectiles. International Journal of Naval Architecture and Ocean Engineering, 13, 450-465.

[4] O'Connor, J., & Rogers, B. D. (2021). A fluid-structure interaction model for free-surface flows and flexible structures using smoothed particle hydrodynamics on a GPU. Journal of Fluids and Structures, 104, 103312.

[5] Zhang, Q., Zong, Z., Sun, T. Z., et al. (2021). Characteristics of cavity collapse behind a high-speed projectile entering the water. Physics of Fluids, 33(6), 062110.

[6] Wang, Z., Feng, P., Liu, G., et al. (2022). Load and motion behaviors of ogive-nosed projectile during high-speed water entry with angle of attack. Ocean Engineering, 266, 112937.

[7] Yu, Y., Shi, Y., Pan, G., et al. (2022). Effect of asymmetric nose shape on the cavity and mechanics of projectile during high-speed water entry. Ocean Engineering, 266, 112983.

[8] Sun, T., Shen, J., Jiang, Q., et al. (2022). Dynamics analysis of high-speed water entry of axisymmetric body using fluid-structure-acoustic coupling method. Journal of Fluids and Structures, 111, 103551.

[9] Nguyen, V. T., & Park, W. G. (2022). Numerical study of the thermodynamics and supercavitating flow around an underwater high-speed projectile using a fully compressible multiphase flow model. Ocean Engineering, 257, 111686.

[10] Lu, L., Yan, X., Li, Q., et al. (2022). Numerical study on the water-entry of asynchronous parallel projectiles at a high vertical entry speed. Ocean Engineering, 250, 111026.

[11] Liu, X., Luo, K., Yuan, X., et al. (2023). Numerical study on the impact load characteristics of a trans-media vehicle during high-speed water entry and flat turning. Ocean Engineering, 273, 113986.

[12] Sui, Y. T., Ming, F. R., Wang, S. P., et al. (2023). Experimental investigation on the impact force of the oblique water entry of a slender projectile with spring buffer. Applied Ocean Research, 138, 103631.

[13] Tavakoli, S., Mikkola, T., & Hirdaris, S. (2023). A fluid-solid momentum exchange method for the prediction of hydroelastic responses of flexible water entry problems. Journal of Fluid Mechanics, 965, A19.

[14] Li, Z., Hu, H., Wang, C., et al. (2024). Hydrodynamics and stability of oblique water entry in waves. Ocean Engineering, 292, 116506.

[15] Wang, C., Huang, Q., Lu, L., et al. (2024). Numerical investigation of water entry characteristics of a projectile in the wave environment. Ocean Engineering, 294, 116821.

[16] Che, P., Shi, Y., Zhao, H., et al. (2024). Study on the cavity evolution and load characteristics of large projectile during high-speed water entry. Ocean Engineering, 303, 117673.

[17] Hao, C., Dang, J., Huang, C., et al. (2024). Investigation of oblique water entry of high-speed supercavitating projectiles using transient fluid-structure interaction simulation. Ocean Engineering, 303, 117702.

[18] Huang, Q., Wang, C., Shi, Y., et al. (2024). Study of the cavity and hydrodynamic characteristics of water entry for projectiles with different wave parameters. Ocean Engineering, 313, 119441.

[19] Yang, L., Zhang, A. M., Liu, Y., et al. (2024). Compressibility effects on cavity dynamics and shock waves in high-speed water entry. Physics of Fluids, 36(4), 042104.

[20] Hu, X., Wei, Y., & Wang, C. (2024). Effect of fluid-structure interaction on the oblique water entry of the projectile under the influence of floating ice structure. Physics of Fluids, 36(4), 043331.

[21] Yan, X., Liu, R., Huo, B., et al. (2024). Numerical investigation of sequential water entry for two projectiles at varied entry angles. Physics of Fluids, 36(6), 063319.

[22] Zhou, B., Zhao, Z., Dai, Q., et al. (2024). Numerical study on the cavity dynamics of water entry and exit for a high-speed projectile crossing a wave. Physics of Fluids, 36(6), 063321.

[23] Peng, T. S., Peng, Y. X., Sun, P. N., et al. (2024). Mitigating impact loads during water entry by utilizing the air-spring effect. Ocean Engineering, 308, 118260.

[24] Wang, S., Jiang, Y., Zou, Z., et al. (2025). Experimental investigation of a body water entry with a water jet cavitator. Journal of Marine Science and Application, 24(2), 388-397.

[25] Chen, J., Yang, P., Li, J., et al. (2025). Deflection law in trajectory of large caliber conical-nosed projectile at high-speed oblique water entry. Physics of Fluids, 37(3), 034126.